frontiers | Frontiers in Bioengineering and Biotechnology

TYPE Original Research
PUBLISHED 20 March 2025
DOI 10.3389/fbioe.2025.1566946

OPEN ACCESS

EDITED BY
Xianzhi Zhang,
Yale University, United States

REVIEWED BY
Fei Chang,
University of Shanghai for Science and Technology, China
Yaxiong Tian,
Guilin University of Technology, China

*CORRESPONDENCE
Ye-Fu Liu,
hy8151@163.com

RECEIVED 26 January 2025
ACCEPTED 05 March 2025
PUBLISHED 20 March 2025

CITATION
Liu F-Y, Wang X and Liu Y-F (2025) Preparation of $La_2(WO_4)_3/CuWO_4$ composite nanomaterials with enhanced sonodynamic anti-glioma activity.
Front. Bioeng. Biotechnol. 13:1566946.
doi: 10.3389/fbioe.2025.1566946

Preparation of $La_2(WO_4)_3/CuWO_4$ composite nanomaterials with enhanced sonodynamic anti-glioma activity

Fang-Yu Liu[1], Xin Wang[2] and Ye-Fu Liu[3]*

[1]The First Clinical College, Liaoning University of Traditional Chinese Medicine, Shenyang, China, [2]Shenyang Key Laboratory for Causes and Drug Discovery of Chronic Diesases, Liaoning University, Shenyang, China, [3]Liaoning Cancer Hospital and Institute, Shenyang, China

Introduction: Sonodynamic therapy (SDT) is an innovative way to treat tumors by activating sonosensitizers via ultrasound (US). The development of sonosensitizers with high sonodynamic activity is the key to promote the clinical application of SDT.

Methods: In this study, a novel sonosensitizer, $La_2(WO_4)_3/CuWO_4$ composite LC-10, was prepared by two-step hydrothermal method and characterized. In addition, the sonodynamic antitumor activity of $La_2(WO_4)_3/CuWO_4$ composite LC-10 was investigated using u251 glioma cells as a model.

Results and Discussion: The results showed that compared with $La_2(WO_4)_3$ and $CuWO_4$, $La_2(WO_4)_3/CuWO_4$ composite had better sonodynamic antitumor activity, and LC-10 had good biosafety at concentrations below 50 μg/mL. After $La_2(WO_4)_3$ and $CuWO_4$ formed $La_2(WO_4)_3/CuWO_4$ composite, the recombination of electron-hole ($e^- - h^+$) pairs were effectively inhibited, and more strongly oxidizing ROS was produced, inducing apoptosis of u251 glioma cells. In which, singlet oxygen ($^1O_2$) and hydroxyl radical (·OH), especially the production of ·OH, played an important role in the $La_2(WO_4)_3/CuWO_4$ composite mediated SDT antitumor process. The results of this study would offer a foundation for the design of $CuWO_4$ base nano-sonosensitizers and its further clinical application in SDT antitumor. In addition, it also provided a new strategy for the design and development of novel nano-sonosensitizers with excellent sonodynamic activity.

KEYWORDS

$La_2(WO_4)_3/CuWO_4$ composite, nano-sonosensitizer, sonodynamic therapy (SDT), sonodynamic antitumor activity, reactive oxygen species (ROS)

1 Introduction

Sonodynamic therapy (SDT) is an emerging non-invasive cancer treatment derived from photodynamic therapy (PDT) (Canavese et al., 2018). SDT uses the focusing of ultrasound (US) and strong penetration of biological tissues to enrich tumor sites of sonosensitizers with certain frequency and intensity of US, and activates the sonosensitizers to produce cytotoxicity, thus producing antitumor effects (Rosenthal et al., 2004). In 1993, Umemura et al. (Umemura et al., 1993) named this method of combining sonosensitizer with US for tumor treatment as SDT according to the name of PDT. This method not only gets rid of the disadvantage of PDT's poor tissue permeability (Hachimine et al., 2007a), but

also shows unique advantages in the non-invasive treatment of deep tumors due to its local cytotoxic effect, which can minimize the damage of normal tissues around the tumor site (Yang et al., 2021). Therefore, SDT has attracted wide attention since it was proposed (Han et al., 2018; Wu et al., 2022).

According to the action mechanisms of SDT, the performance of sonosensitizers plays a crucial role in the SDT process. The traditional organic sonosensitizers used in early studies mainly include hematoporphyrin (Hp) (Umemura et al., 1989) and its derivatives such as ATX-70 (Sasaki et al., 1998), DCPH-P-Na(I) (Hachimine et al., 2007b), haematoporphyrin monomethyl ether (HMME) (Li et al., 2008) and protoporphyrin IX (PPIX) (Liu et al., 2006). In addition, some antitumor drugs and small molecule drugs such as curcumin (Jiang et al., 2020), acridine orange (Xing et al., 2021), methylene blue (He et al., 2015a), promethazine hydrochloride (He et al., 2011a), dioxypromethazine hydrochloride (He et al., 2011b), eosin B (He et al., 2015b), brilliant cresyl blue (Wang et al., 2018), toluidine blue and azure A (Qian et al., 2024) have also been proved to have good sonodynamic activity. The advantages of these organic sonosensitizers are that they all have clear chemical structures and excellent biodegradation rates. However, most of them have disadvantages such as greater hydrophobicity and phototoxicity, as well as lower tissue selectivity and stability when applied *in vivo* (Wu et al., 2022; Xing et al., 2021).

In recent decades, the research of inorganic nanoparticle based sonosensitizers such as titanium dioxide (TiO_2) has made great progress (Yang et al., 2021). Compared with organic small molecule drugs, inorganic nanomaterials have the advantages of excellent physical and chemical properties, easy manufacturing, low phototoxicity, good biocompatibility and stability (Yang et al., 2021; Li et al., 2023). At the same time, various inorganic nanomaterials such as $TiH_{1.924}$ (Gong et al., 2020), $BaTiO_3$ (Zhu et al., 2020) and Bi_2MoO_6 (Dong et al., 2021) were proved to have good sonodynamic activity. These inorganic nano-sonosensitizers absorb the energy generated by the US cavitation effect (thermal and sonoluminescence) and excite the sonosensitizers to produce electron-hole (e^-–h^+) separation. The separated e^- and h^+ migrate to the surface of the sonosensitizer to produce corresponding reduction and oxidation reactions, resulting in a large number of reactive oxygen species (ROS) generation and antitumor effects (Li et al., 2023). However, due to the rapid recombination of e^- and h^+ in the band structure, the efficiency of ROS generation of single-component sonosensitizer is relatively low, which affects the effect of SDT (Li et al., 2023; Ping et al., 2023). Therefore, the researchers overcome the recombination of carriers by forming oxygen defect layers on the surface of sonosensitizer (Zhou et al., 2022; Wang Y. et al., 2023), deposition of precious metals (Zhang et al., 2021), ion doping (Cheng et al., 2024), construction of heterojunction (Chen et al., 2022; Kang et al., 2022) and a combination of these strategies (Zhang et al., 2023a; Song et al., 2022), thus further improving the efficiency of SDT.

Because of the effective conversion of light energy into thermal and chemical energy, tungstate nanomaterials are often used as photoresponsive materials in the field of photocatalytic degradation of organic pollutants (Kumar et al., 2022), photothermal therapy (Xiao et al., 2016), PDT and radiotherapy (Zhang et al., 2018). $CuWO_4$ is an important semiconductor material with a band gap of about 2.60 eV (Liu et al., 2023). Compared with other tungstate structures, $CuWO_4$ exhibits stronger absorption in the near infrared region, indicating that $CuWO_4$ is a good candidate for PDT. For example, Cui et al. (2021) prepared a single original nanostructured $CuWO_4$ nanodots, and introduced the nanodots into tumor tissue to generate ROS to generate PDT under 808 nm light irradiation, and released copper ions into the acidic tumor microenvironment to promote Fenton-like reaction and generate chemodynamic therapy, which can effectively inhibit tumor tissue growth. Since most sonosensitizers are derived from photosensitizers, $CuWO_4$ nanomaterials may be a candidate sonosensitizer for SDT applications.

The construction of heterojunction can effectively inhibit the e^-–h^+ pairs recombination, promote the generation of ROS, and significantly improve the effect of SDT (Ping et al., 2023; Chen et al., 2022; Kang et al., 2022). Therefore, in this paper, $La_2(WO_4)_3$/$CuWO_4$ composites were prepared by two-step hydrothermal method, and the microstructure, morphology and elemental composition of $La_2(WO_4)_3$/$CuWO_4$ composites were analyzed by X-ray diffraction (XRD), scanning electron microscope (SEM), energy dispersive X-ray spectroscopy (EDX) and X-ray photoelectron spectroscopy (XPS). Using u251 glioma cells as model, the sonodynamic anti-glioma activity of $La_2(WO_4)_3$/$CuWO_4$ composites was investigated by MTT method. Finally, the sonodynamic antitumor mechanism of $La_2(WO_4)_3$/$CuWO_4$ composites was discussed based on the optical properties and electrochemical characteristics of $La_2(WO_4)_3$/$CuWO_4$ composites and ROS probe experimental results. It is expected that the results of this study will provide the research basis for the further development and application of $CuWO_4$ based sonosensitizers in SDT antitumor.

2 Experimental sections

2.1 Materials and reagents

$NaWO_4{\cdot}2H_2O$ (AR), 1, 3-diphenylisobenzofuran (DPBF, AR) and terephthalic acid (TA, AR) were purchased from Tianjin Hengxing Chemical reagent manufacturing Co., LTD., (China). NaOH (AR) was purchased from Tianjin Yongda Chemical reagent Co., LTD., (China). Anhydrous ethanol (AR), $Cu(NO_3)_2{\cdot}3H_2O$ and $La(NO_3)_3{\cdot}6H_2O$ were purchased from Tianjin Damao chemical reagent factory (China). Phosphate buffer (PBS, BR), thiazole blue (AR), RPMI Medium 1640 (BR), superior fetal bovine serum (BR), 0.25% trypsin/EDTA digestion solution (BR), serum-free cryopreservation (BR), dimethyl sulfoxide (DMSO, BR), 3-(4,5-dimethylthiazol-2-yl)-2,5 diphenyl-tetrazolium bromide (MTT, BR) and AO/EB Kit (LR) were purchased from Beijing Solarbio Technology Co., LTD., (China). Human glioma u251 cells were purchased from Cell Resource Center, Institute of Basic Medicine, Chinese Academy of Medical Sciences.

2.2 Preparation of $La_2(WO_4)_3$/$CuWO_4$ composite

1.0872 g $Cu(NO_3)_2{\cdot}3H_2O$ and 0.2165 g $La(NO_3)_3{\cdot}6H_2O$ were dissolved together in 40 mL deionized water. 2.3090 g

$Na_2WO_4{\cdot}_2H_2O$ was weight and dissolved in 20 mL deionized water. Then, under the condition of magnetic stirring, the Na_2WO_4 solution was added to the mixed solution of $Cu(NO_3)_2$ and $La(NO_3)_3$ drop by drop, and continued to stir for 30 min. Then the mixed solution was transferred to the polytetrafluoroethylene inner tank of 100 mL stainless steel reactor and reacted in a constant temperature drying oven at 180°C for 24 h. The reaction products were washed with deionized water and anhydrous ethanol three times respectively, and dried at 60°C for 8 h to obtain $La_2(WO4)_3$/$CuWO_4$ composite (LC-10) sample. According to the above experimental methods, $CuWO_4$ sample was prepared without adding $La(NO_3)_3{\cdot}6H_2O$ in the process of synthesis. Similarly, $La_2(WO_4)_3$ sample was prepared under the above experimental conditions without adding $Cu(NO_3)_2{\cdot}3H_2O$ in the process of synthesis. Detailed information on the various instruments used in the paper could be found in Supplementary Material.

2.3 Cytotoxicity assay

The cytotoxicity of nano-sonosensitizers and nano-sonosensitizers-mediated sonodynamic action on u251 glioma cells was tested by the typical MTT assay. The u251 glioma cells were plated in 96-well microplates (6×10^3 cells per well) and incubated at 37°C for 24 h. After removing the culture medium, 50 μL of base medium containing various concentrations of $La_2(WO_4)_3$, $CuWO_4$ and LC-10 samples (10, 20, 50, 100 and 200 μg/mL) were added. After incubation at 37°C for 24 h, 20 μL of medium containing MTT (0.5 mg/mL diluted with medium) was added to each well and continued incubation at 37°C for 4 h. Then, the supernatant in the well was discarded, 150 μL of DMSO was added to each well, and the optical density (OD) was measured at 490 nm using a microplate reader instrument. The cell viability was calculated by Graphpad Pism software. In the experiment on sonodynamic damage to u251 glioma cells, various concentrations of $La_2(WO_4)_3$, $CuWO_4$ and LC-10 samples (0, 10, 20, 30, 40 and 50 μg/mL) were added. After incubation at 37°C for 24 h, the cells were irradiated with a 1.0 MHz US probe for 1 min, and incubated at 37°C for 24 h. MTT assay was used to detect cell viability.

2.4 Detection of ROS

In order to detect the formation of singlet oxygen ($^1O_2$) in the SDT process, DPBF was used as a probe, which could react with $^1O_2$ to decompose DPBF into 1, 2-diphenyl-benzene, resulting in a decrease in the absorption intensity of its characteristic absorption peak at 410 nm (Zhou et al., 2024; Zhang et al., 2023b). The specific experimental method was as follows: 8 mL of 75% ethanol solution containing DPBF (8 mg/L) and sonosensitizer (20 μg/mL) were taken and placed in the US device for 5 min. Then centrifuged at 15,000 rpm for 10 min to remove the sonosensitizer. The absorption spectra of the solution near 410 nm were measured with an ultraviolet-visible (UV-Vis) spectrophotometer.

In order to detect the formation of hydroxyl radical (·OH) in the SDT process, TA was used as a probe, which could react with ·OH to produce 2-hydroxyterephthalic acid, resulting in a characteristic fluorescence emission peak generated around 430 nm (Pan et al., 2018). Typically, 8 mL 0.5 mmol/L TA solution containing 20 μg/mL of sonosensitizer was taken, then the solution was placed in US bath for US irradiation for 5 min, and centrifugated at 15,000 rpm for 10 min to remove the sonosensitizer. The emission spectrum of the supernatant near 425 nm was measured by a fluorescence spectrophotometer with excitation wavelength of 315 nm.

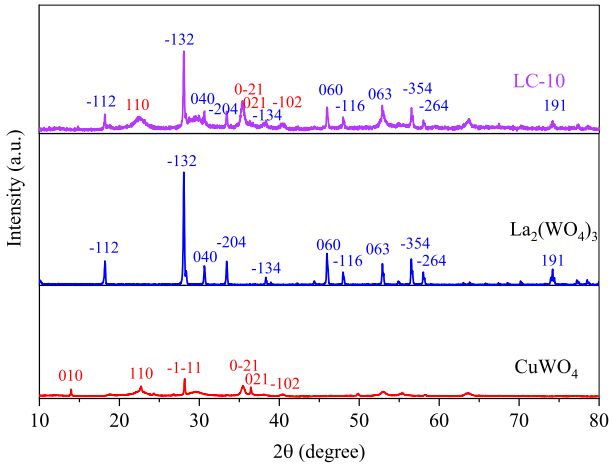

FIGURE 1
XRD patterns of the prepared $La_2(WO_4)_3$, $CuWO_4$ and LC-10 composite.

2.5 Statistical analysis

All data were expressed as mean ± SD, and one-way ANOVA was performed by Graphpad Pism software. When P was less than 0.05, it was statistically significant.

3 Results and discussions

3.1 Characterization of $La_2(WO_4)_3$/$CuWO_4$ composite

The XRD patterns of the prepared $La_2(WO_4)_3$, $CuWO_4$ and LC-10 composite were shown in Figure 1. As shown in Figure 1, the XRD patterns of $CuWO_4$ showed that the diffraction peaks were at 13.96°, 22.73°, 28.17°, 35.46°, 36.43° and 40.52°, which belonged to the (010), (110), (−1−11), (0−21), (021) and (−102) planes of $CuWO_4$, respectively. For $La_2(WO_4)_3$, the diffraction peaks at 18.20°, 28.08°, 30.64°, 33.44°, 38.34°, 45.98°, 47.98°, 52.92°, 56.52°, 58.02° and 74.20° were related to the planes (−112), (−132), (040), (−204), (−134), (060), (−116), (063), (−354), (−264) and (191) of $La_2(WO_4)_3$. For LC-10 composite, a series of characteristic peaks of $CuWO_4$ and $La_2(WO_4)_3$ appeared. The XRD diffraction peaks at 22.52°, 35.40°, 36.32° and 40.50° were attributed to the (110), (0-21), (021) and (−102) crystal planes of $CuWO_4$. The XRD diffraction peaks at 18.22°, 28.10°, 30.68°, 33.44°, 38.32°, 45.98°, 47.98°, 52.90°, 56.54°, 58.02° and 74.20° were attributed to the (−112), (−132), (040),

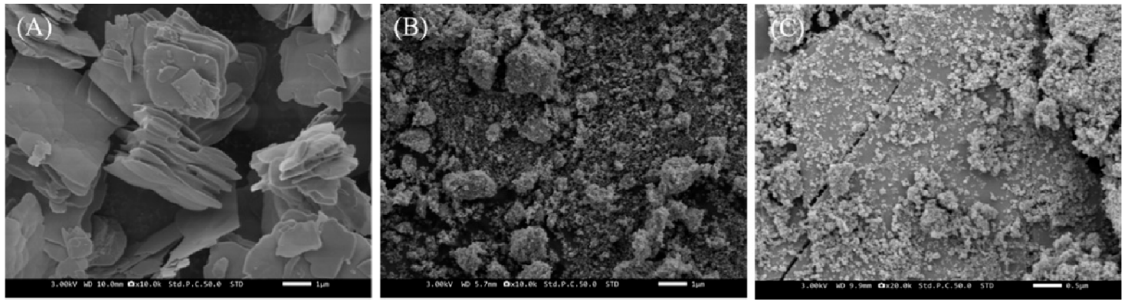

FIGURE 2
SEM images of synthesized $La_2(WO_4)_3$ **(A)**, $CuWO_4$ **(B)** and LC-10 **(C)** samples.

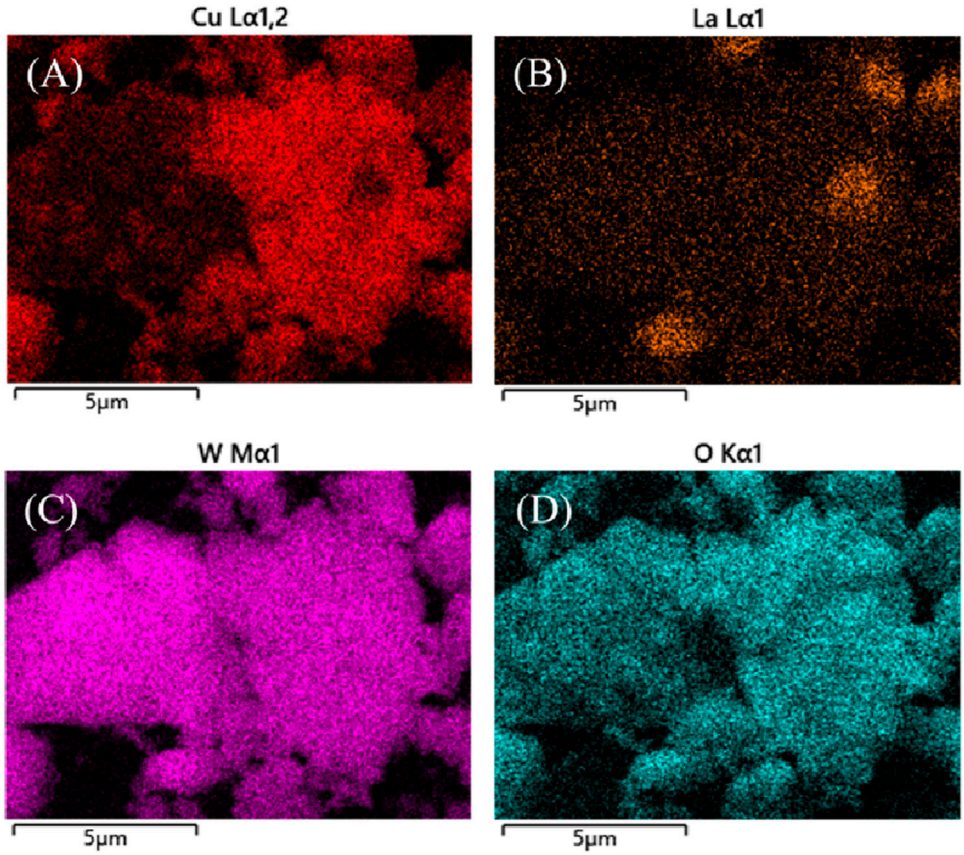

FIGURE 3
EDX diagrams of **(A)** Cu, **(B)** La, **(C)** W and **(D)** O elements in the synthesized LC-10 sample.

(−204), (−134), (060), (−116), (063), (−354), (−264) and (191) crystal planes of $La_2(WO_4)_3$. The above results confirmed the successful preparation of $La_2(WO_4)_3/CuWO_4$ composite.

The morphologies of the prepared $La_2(WO_4)_3$, $CuWO_4$ and LC-10 samples were analyzed by SEM, and the results were shown in Figure 2. It could be seen that the prepared $La_2(WO_4)_3$ sample had an irregular lamellar structure (Figure 2A), and the prepared $CuWO_4$ sample had a nanoparticle shape (Figure 2B). It could be seen from the SEM image of the prepared LC-10 sample (Figure 2C) that $CuWO_4$ nanoparticles were evenly distributed on the lamellar structure of $La_2(WO_4)_3$, which proved the successful composite of $La_2(WO_4)_3$ and $CuWO_4$. The EDX diagrams of Cu, La, W and O elements in the synthesized LC-10 sample were shown in Figure 3. It could be seen that Cu, La, W and O elements were evenly distributed on the surface of the synthesized LC-10 sample.

The elemental compositions and chemical valence states of synthesized $La_2(WO_4)_3$, $CuWO_4$ and LC-10 samples were analyzed by XPS measurement. As shown in Figure 4A, the three peaks of $La_2(WO_4)_3$ sample at 832.2, 32.6 and 527.7 eV were attributed to La 3*d*, W 4*f* and O 1*s*, respectively. As shown in

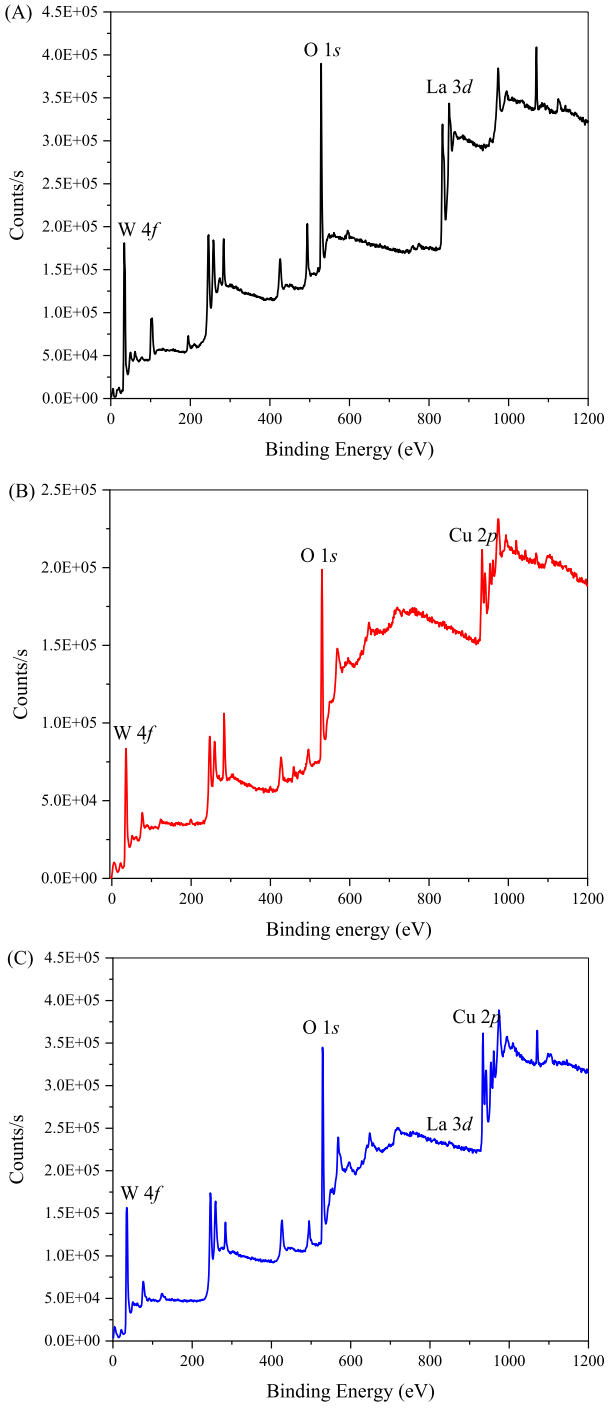

FIGURE 4
XPS spectra of synthesized $La_2(WO_4)_3$ **(A)**, $CuWO_4$ **(B)** and LC-10 **(C)** samples.

Figure 4B, the three peaks of the $CuWO_4$ sample at 932.2, 31.1 and 528.1 eV were attributed to Cu 2*p*, W 4*f* and O 1*s*, respectively. As shown in Figure 4C, the four peaks of LC-10 composite at 833.3, 932.5, 33.7 and 528.1 eV were attributed to La 3*d*, Cu 2*p*, W 4*f* and O 1*s*, respectively.

The high-resolution XPS spectra of Cu 2*p*, W 4*f*, O 1*s* and La 3*d* in the synthesized $CuWO_4$, $La_2(WO_4)_3$ and LC-10 samples were shown in Figure 5. The two peaks with binding energies of 933.12 and 952.90 eV in the spectrum of Cu 2*p* of $CuWO_4$ (Figure 5A) belonged to Cu $2p_{3/2}$ and Cu $2p_{2/1}$, respectively, which suggested that the presence of Cu^{2+} and the capture of photogenerated electrons by Cu^{2+} may cause the valence state change from Cu(II) to Cu(I) (Wang X. et al., 2023; Wan et al., 2013). Compared with $CuWO_4$, the two fitted peaks of Cu 2*p* of LC-10 composite sample shifted slightly to the higher energy, located at 933.57 and 953.36 eV, respectively. In the high resolution XPS spectrum of W 4*f* of $CuWO_4$ (Figure 5B), the two peaks at the binding energies of 33.83 and 35.97 eV belonged to W $4f_{7/2}$ and W $4f_{5/2}$, respectively, suggesting the existence of W^{6+} in the synthesized sample (Wang et al., 2021; Xu et al., 2023). The two fitted peaks of W 4*f* of $La_2(WO_4)_3$ were located at 33.73 and 35.89 eV, respectively. Compared with $CuWO_4$ and $La_2(WO_4)_3$, the two fitted peaks of W 4*f* of LC-10 composite sample shifted slightly to the higher energy, located at 34.07 and 36.18 eV, respectively. The high-resolution XPS spectra of O 1*s* of $CuWO_4$ shown in Figure 5C displayed two fitted peaks at 528.73 and 529.83 eV, respectively, indicating the presence of the lattice oxygen and O-H bonds absorbed on surface of the synthesized sample (He et al., 2024; Wei et al., 2023). The two fitted peaks of O 1*s* of $La_2(WO_4)_3$ were located at 528.85 and 531.16 eV, respectively. Compared with $CuWO_4$ and $La_2(WO_4)_3$, the two fitted peaks of O 1*s* of LC-10 composite sample shifted slightly to the higher energy or lower energy, located at 529.01 and 530.29 eV, respectively. The high-resolution XPS spectrum of La 3*d* of $La_2(WO_4)_3$ shown in Figure 5D displayed the spin–orbit splitting: La $3d_{5/2}$ (833.51 and 836.97 eV) and La $3d_{3/2}$ (850.28 and 854.00 eV), which were in accordance with the standard XPS peaks of La^{3+} (Baby et al., 2024). Compared with $La_2(WO_4)_3$, the fitted peaks of La 3*d* of LC-10 composite sample also shifted slightly. The above results indicated that the two substances, $CuWO_4$ and $La_2(WO_4)_3$ interacted with each other, and the heterojunction of $La_2(WO_4)_3/CuWO_4$ formed.

The UV-Vis diffuse reflectance spectra (DRS) of $CuWO_4$, $La_2(WO_4)_3$ and LC-10 were measured using a UV-Vis spectrophotometer in the wavelength range of 200–800 nm, and the results were shown in Figure 6. It could be seen that $CuWO_4$ had a strong light absorption capacity in the entire 200–800 nm range, indicating that $CuWO_4$ had a good light response ability to both UV and Vis light. $La_2(WO_4)_3$ had an obvious absorption boundary near 340 nm, which indicated that $La_2(WO_4)_3$ had a strong absorption capacity for UV light. It could be seen from the DRS of LC-10 that $La_2(WO_4)_3/CuWO_4$ composite had a good light response to both UV and Vis light. Based on the above DRS results, the band gap energy (E_g) of $CuWO_4$ and $La_2(WO_4)_3$ could be obtained by the Kubelka-Munk formula (Wang et al., 2021). The correlation curves of $(Ahv)^2$ vs. hv of $CuWO_4$ and $La_2(WO_4)_3$ were shown in Figures 7A, B, the *Eg* of $CuWO_4$ and $La_2(WO_4)_3$ were obtained as 2.99 and 2.54 eV, respectively.

3.2 Sonodynamic anti-glioma activity of $La_2(WO_4)_3/CuWO_4$ composite

First, the cytotoxicity of prepared $CuWO_4$, $La_2(WO_4)_3$ and LC-10 samples to u251 cells was investigated. In the presence of different concentrations (10, 20, 50, 100 and 200 μg/mL) prepared $CuWO_4$, $La_2(WO_4)_3$ and LC-10 samples, the cell viability of u251 cells during

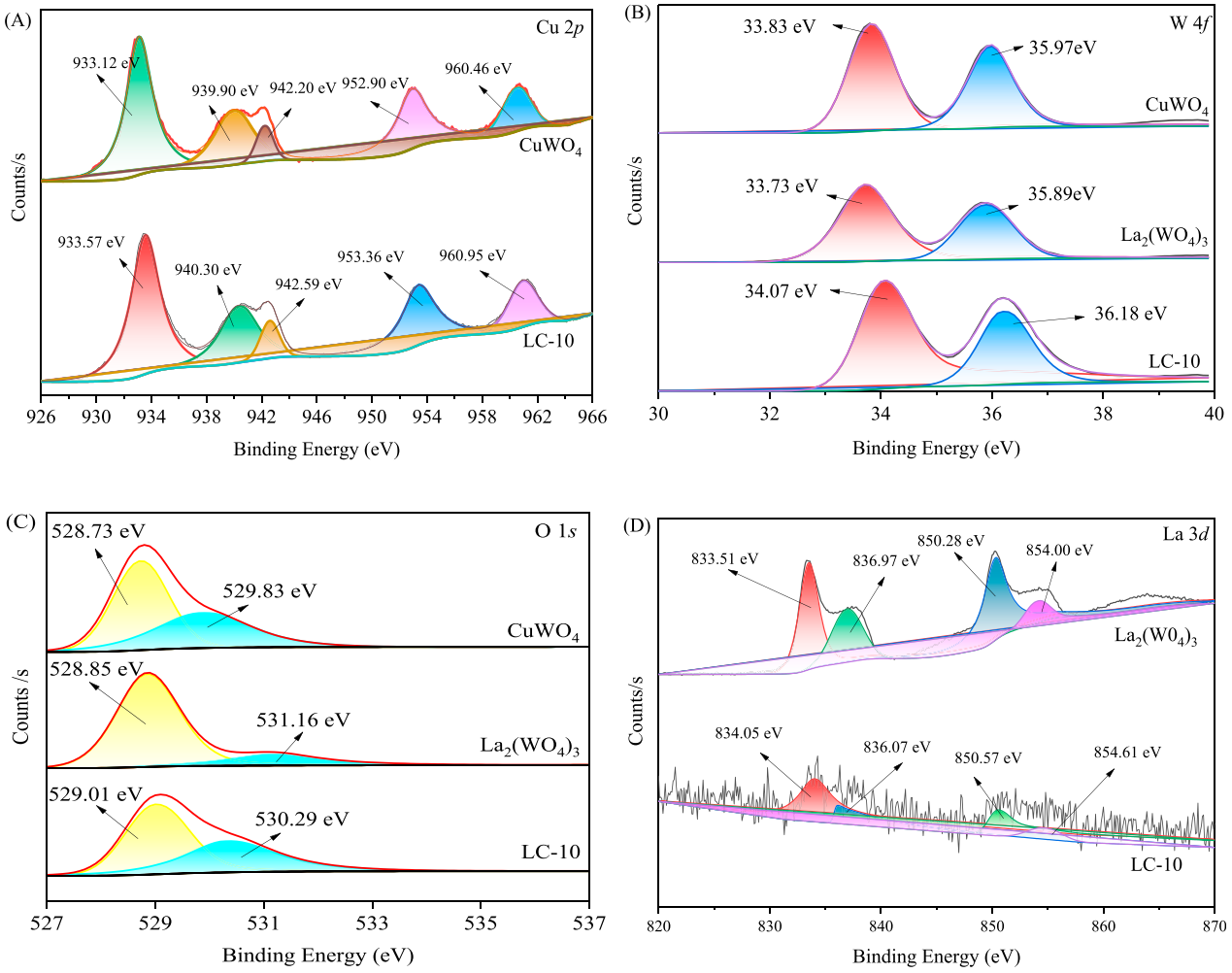

FIGURE 5
High-resolution XPS spectra of Cu 2*p* **(A)**, W 4*f* **(B)**, O 1*s* **(C)** and La 3*d* **(D)** in synthesized $CuWO_4$, $La_2(WO_4)_3$ and LC-10 samples.

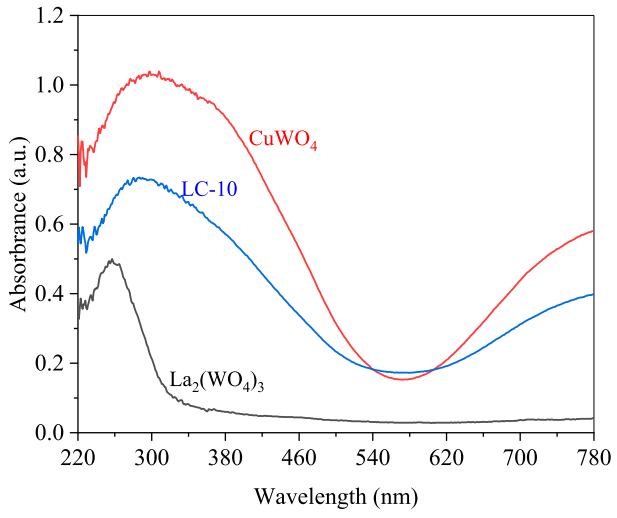

FIGURE 6
DRS spectra of $CuWO_4$, $La_2(WO_4)_3$ and LC-10 samples.

logarithmic growth was measured by MTT method. Figure 8A displayed the cytotoxicity test results of $CuWO_4$. When $CuWO_4$ concentration was 10, 20, 50, 100 and 200 μg/mL, the cell viability was 105.45% ± 5.05%, 103.01% ± 2.57%, 96.31% ± 3.71%, 93.50% ± 6.46% and 86.65% ± 8.08%, respectively. Figure 8B showed the cytotoxicity test results of $La_2(WO_4)_3$. When the concentration of $La_2(WO_4)_3$ was 10, 20, 50, 100 and 200 μg/mL, the cell viability was 97.72% ± 4.54%, 93.66% ± 4.80%, 90.84% ± 2.78%, 89.88% ± 4.15% and 85.65% ± 6.49%, respectively. The results showed that $CuWO_4$ and $La_2(WO_4)_3$ did not cause obvious cytotoxicity to u251 cells when the concentrations of $CuWO_4$ and $La_2(WO_4)_3$ were below 200 μg/mL. Figure 8C showed the cytotoxicity test results of LC-10 sample. When the concentration of LC-10 was 10, 20, 50, 100 and 200 μg/mL, the cell viability was 95.17% ± 4.35%, 94.40% ± 6.70%, 84.11% ± 5.31%, 79.26% ± 4.38% and 71.05% ± 6.12%, respectively. These results showed that with the increase of LC-10 concentration, the cell survival rate decreased gradually. When the concentration of LC-10 was higher than 50 μg/mL, it had a certain toxic effect on cells.

Next, u251 cells were treated differently to evaluate the sonodynamic therapeutic effect of $La_2(WO_4)_3/CuWO_4$ composite on tumor cells. It could be seen from Figure 9A that the cell viability

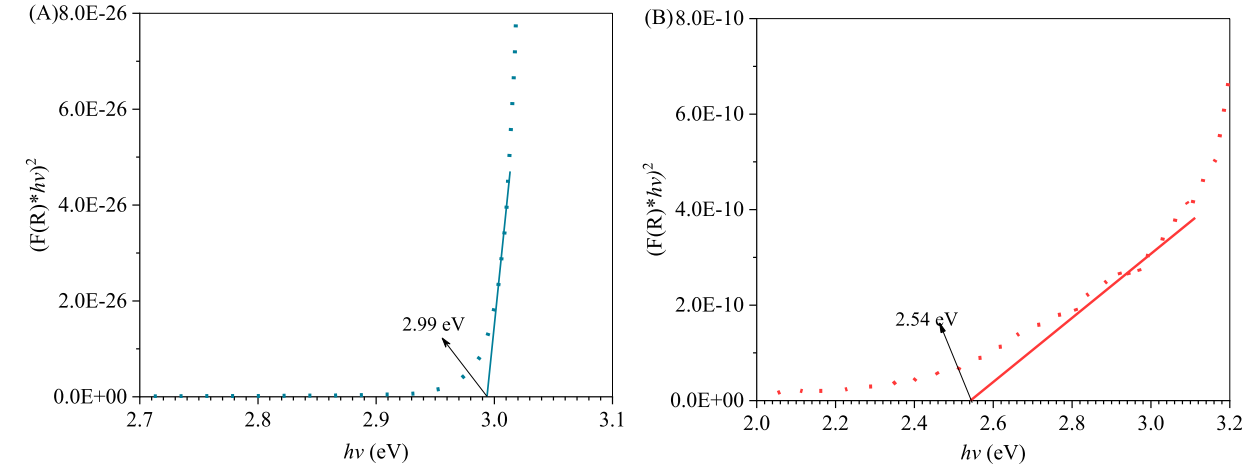

FIGURE 7
Correlation curves of $(Ah\nu)^2$ vs. $h\nu$ of $CuWO_4$ **(A)** and $La_2(WO_4)_3$ **(B)**.

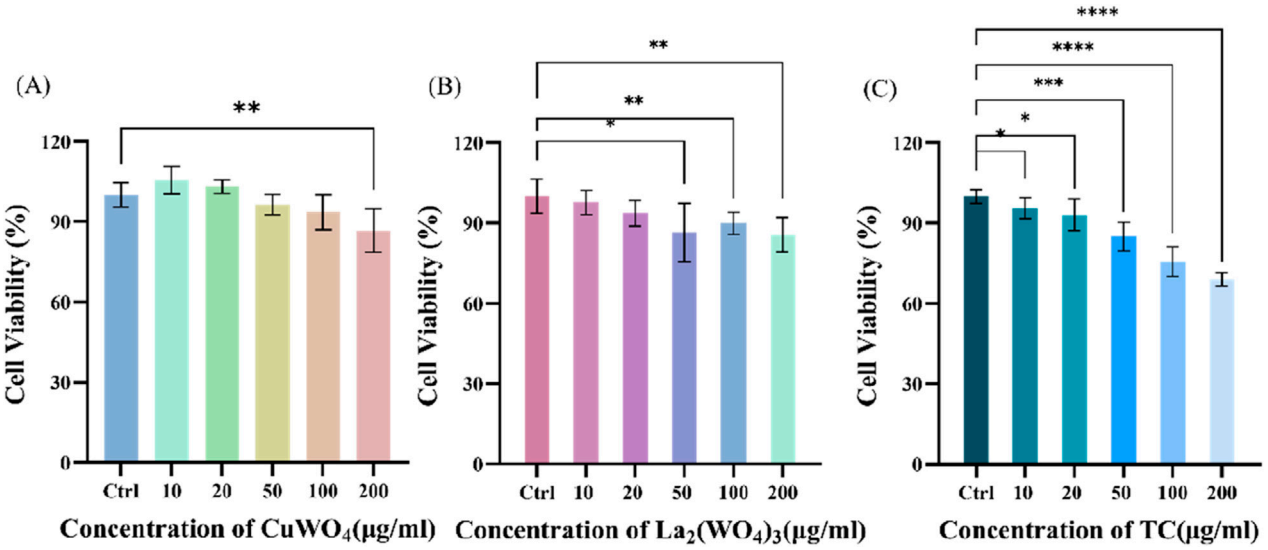

FIGURE 8
Cytotoxicity of $CuWO_4$ **(A)**, $La_2(WO_4)_3$ **(B)** and LC-10 **(C)** to u251 cells (*p < 0.05,**p < 0.01,***p < 0.001,****p < 0.0001).

decreased slightly under US irradiation alone. This was because the energy generated by the cavitation effect of US could lead to the cracking of water molecules, resulting in a strong oxidizing ·OH. The effects of different concentrations of LC-10 on the cell viability of u251 cells under US irradiation were shown in Supplementary Figures S1–S5. It could be clearly observed that the cell viability of u251 cells treated with SDT in the presence of LC-10 was significantly lower than that treated with LC-10 alone and US alone at any concentration of LC-10. These results suggested that $La_2(WO_4)_3/CuWO_4$ composite had excellent sonodynamic antitumor performance. The cell inhibition rate of u251 cells after SDT in the presence of different concentrations of $CuWO_4$, $La_2(WO_4)_3$ and LC-10 were shown in Figure 9B. It could be seen that the cell inhibition rate of u251 cells after SDT in the presence of LC-10 at any concentration was significantly higher than that in the presence of $CuWO_4$ and $La_2(WO_4)_3$ at same concentration. These results indicated that $La_2(WO_4)_3/CuWO_4$ composite had higher sonodynamic antitumor performance. In addition, it was also shown that the construction of heterojunction was an effective means to improve the sonodynamic antitumor performance of nano-sonosensitizers.

Subsequently, sonodynamic-induced cancer cell apoptosis was further evaluated using AO/EB staining. As shown in Figure 10, under the same experimental conditions, cells were divided into control group (A), US group (B), LC-10 group (C), and LC-10+US group (D). In the control group (Figure 10A), the quantity and intensity of green fluorescence were high, while the orange fluorescence was negligible, indicating good growth of cells. As shown in Figures 10B, C, the US group and the LC-10 group showed weak orange fluorescence, and most of the cells showed

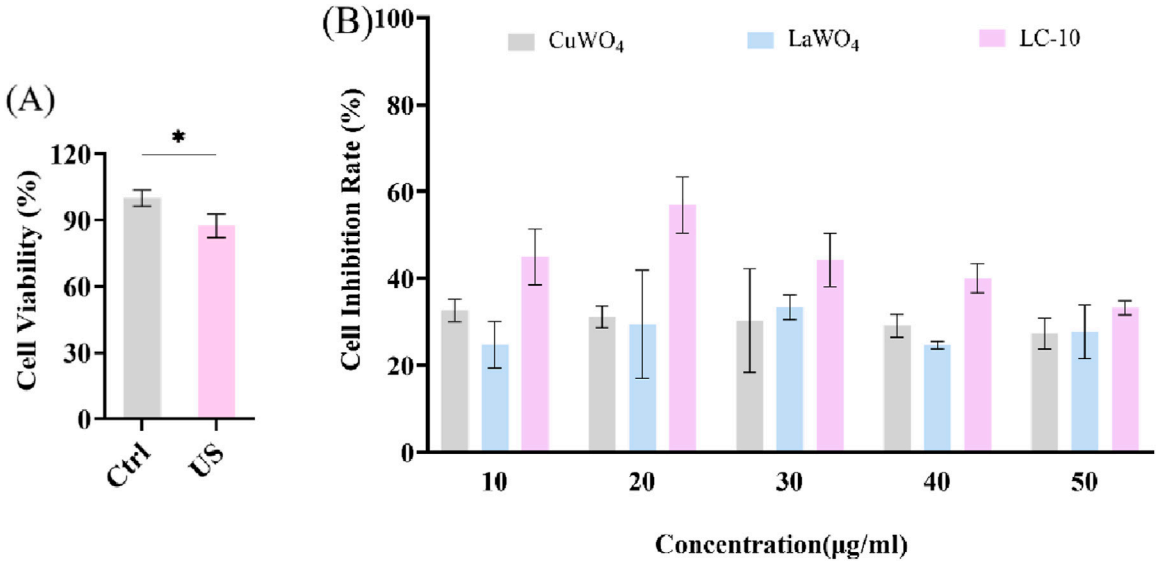

FIGURE 9
Cell viability of u251 cells under US irradiation **(A)** and cell inhibition rate of u251 cells after SDT in the presence of different concentrations of $CuWO_4$, $La_2(WO_4)_3$ and LC-10 **(B)** (*$p < 0.05$).

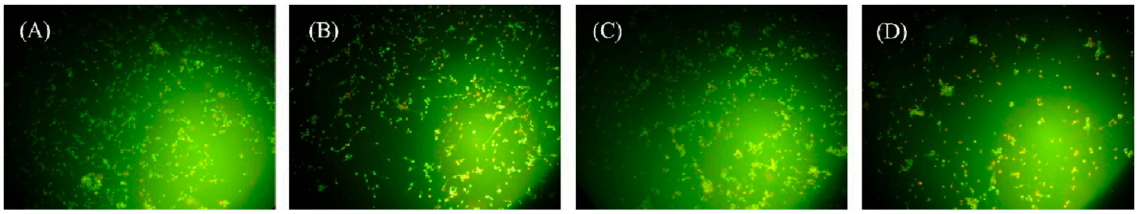

FIGURE 10
Confocal laser scanning microscopy images of u251 cells stained with AO/EB after various treatments. **(A)** control group, **(B)** US group, **(C)** LC-10 group, and **(D)** LC-10+US group.

green fluorescence, indicating that most of the cells had good viability. Figure 10D showed a large amount of orange fluorescence in the LC-10+US group, indicating that LC-10 produced a large number of ROS inducing apoptosis under US irradiation, and the experimental results were consistent with the above MTT results.

3.3 Sonodynamic antitumor mechanism of $La_2(WO_4)_3/CuWO_4$ composite

It could be clearly seen from the above results that the combined use of US and sonosensiizer LC-10 had a much higher inhibitory effect on the growth of u251 glioma cells than that of US alone and LC-10 alone. The combined use of US and sonosensiizer LC-10 also significantly inhibited the growth of u251 glioma cells compared with the combined effect of US and $La_2(WO_4)_3$ and the combined effect of US and $CuWO_4$, indicating that LC-10 had better sonodynamic antitumor activity. The essence of the good sonodynamic activity of the nano-sonosensitizer was that it could become a ROS generator under US irradiation (Duan et al., 2023). In order to study the ability of $La_2(WO_4)_3/CuWO_4$ composite as a sonosensitizer to produce ROS and the corresponding sonodynamic mechanism, specific ROS probes were used to verify the types of ROS produced during SDT process. The $^1O_2$ yields of $La_2(WO_4)_3/CuWO_4$ composite produced under US irradiation were evaluated using DPBF as a probe. It could be seen from Figure 11A, under US irradiation, the absorption peak of DPBF at 410 nm decreased in the presence of LC-10 compared with the control group of water, suggesting the generation of $^1O_2$ in the system. Similarly, the capture of ·OH was tracked by TA. It could be seen from Figure 11B, the combined use of US and LC-10 remarkably increased the fluorescence intensity of the solution around 430 nm. The results showed that $La_2(WO_4)_3/CuWO_4$ composite had good ·OH production ability under US irradiation.

The photoluminescence spectra of $CuWO_4$ and $La_2(WO_4)_3/CuWO_4$ composite LC-10 were measured with a fluorescence spectrophotometer in the wavelength range of 200–600 nm, and the results were shown in Figure 12. It could be seen that under the excitation condition of 269 nm wavelength, $CuWO_4$ had an obvious

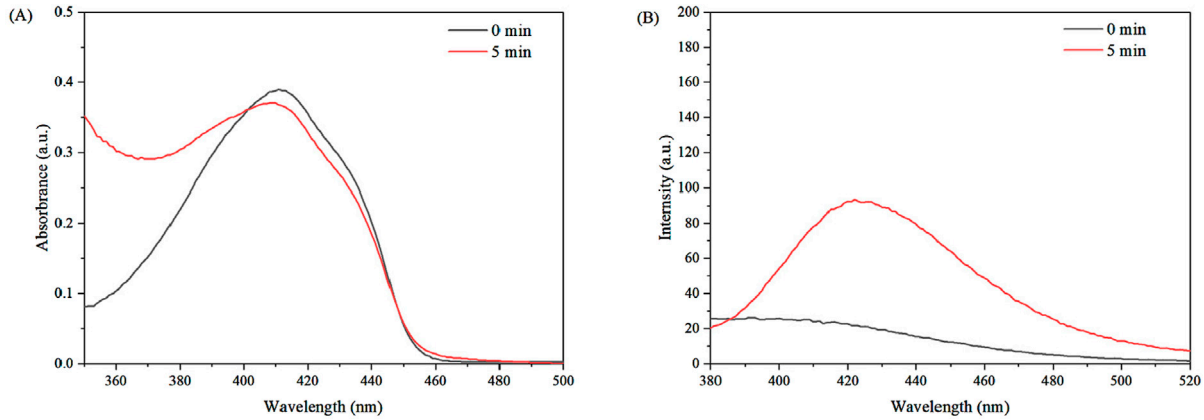

FIGURE 11
Detection of $^1O_2$ **(A)** and ·OH **(B)** in the combined use of US and LC-10 system.

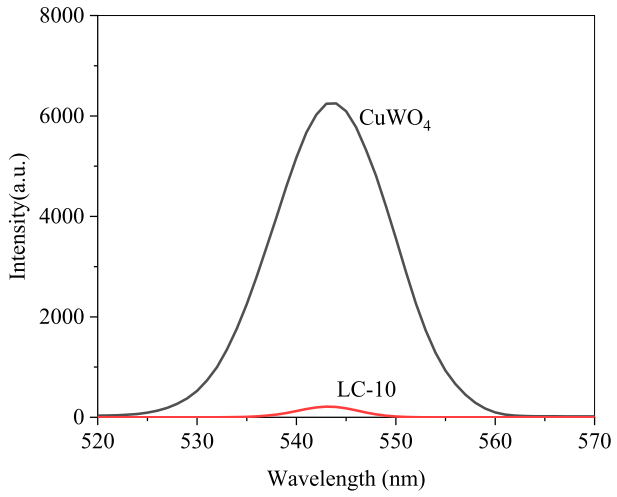

FIGURE 12
Photoluminescence spectra of $CuWO_4$ and LC-10.

emission peak near 520 nm. Similarly, the maximum emission wavelength of the emission peak of LC-10 was also around 520 nm, but its fluorescence intensity was significantly lower than that of $CuWO_4$, indicating that after $La_2(WO_4)_3$ and $CuWO_4$ formed a composite, carrier separation could be effectively realized in the catalyst, and the recombination rate of e^--h^+ pairs was significantly reduced (Liu et al., 2024). The production of ROS of the catalyst under US irradiation was improved significantly, thus displayed excellent sonodynamic antitumor performance.

The type of semiconductor material could be determined by whether the slope of the tangent in the Mott-Schottky curves was positive or negative. A positive slope indicated an n-type semiconductor and a negative slope indicated a p-type semiconductor (Chang et al., 2023; Chang et al., 2024). As seen in Figure 13, The slopes of tangent lines of the Mott-Schottky curves of $La_2(WO_4)_3$ and $CuWO_4$ were both positive. The results showed that all the prepared $La_2(WO_4)_3$ and $CuWO_4$ samples had n-type semiconductor characteristics. Additionally, the flat band potential (E_f) values of the prepared $La_2(WO_4)_3$ and $CuWO_4$ samples could be obtained from the intercept of the tangent with the X-axis (Huang et al., 2024a; Chang et al., 2025). Therefore, the E_f values of $La_2(WO_4)_3$ and $CuWO_4$ samples were determined to be −0.55 V and −0.30 V vs saturated calomel electrode (SCE), respectively. Accordingly, the E_f values of $La_2(WO_4)_3$ and $CuWO_4$ samples could be calculated as −0.31 V and −0.06 V vs standard hydrogen electrode (NHE), considering the correction value between SCE and NHE was 0.24 V (Lu et al., 2025; Huang et al., 2024b). It was known that for most n-type semiconductors, the minimum potential of the conduction band (E_{CB}) was about 0.1–0.3 V lower than the E_f value, and the middle value of 0.2 V was used here (Huang et al., 2024c; Chen et al., 2024). Therefore, the E_{CB} values of $La_2(WO_4)_3$ and $CuWO_4$ samples were calculated as −0.51 V and −0.26 V vs. NHE, respectively. According to the E_g values of $La_2(WO_4)_3$ and $CuWO_4$ samples were 2.54 and 2.99 eV, respectively, and the relationship between the maximum potential of valence band (E_{VB}), E_{CB} and E_g ($E_{VB} = E_{CB} + E_g$) (Han et al., 2025), E_{VB} values of $La_2(WO_4)_3$ and $CuWO_4$ samples relative to NHE could be calculated as 2.03 V and 2.73 V, respectively. Based on the above calculation, the schematic diagram of the band structure corresponding to $La_2(WO_4)_3/CuWO_4$ composite was shown in Figure 14. It could be seen that there are obvious differences in the band and energy level structure between $La_2(WO_4)_3$ and $CuWO_4$ in $La_2(WO_4)_3/CuWO_4$ composite, and a hypothesis that $La_2(WO_4)_3/CuWO_4$ n–n heterojunction formed was proposed.

Combined with the results of the above study and related literature reports, the main mechanism of LC-10-mediated SDT antitumor was proposed (as shown in Figure 14). Firstly, in the process of US irradiation, the tiny bubbles in the liquid were activated by US, resulting in a series of dynamic processes such as expansion, contraction, expansion and collapse, that was, the cavitation effect (Rosenthal et al., 2004; Teng et al., 2024). The cavitation effect (transient cavitation) generated by US could form local hot spots of high temperature and pressure, and its energy could cause water molecules to crack and produced ·OH (Rosenthal et al., 2004), which would cause damage to tumor cells. Secondly, the addition of $La_2(WO_4)_3/CuWO_4$ composite nanoparticles could

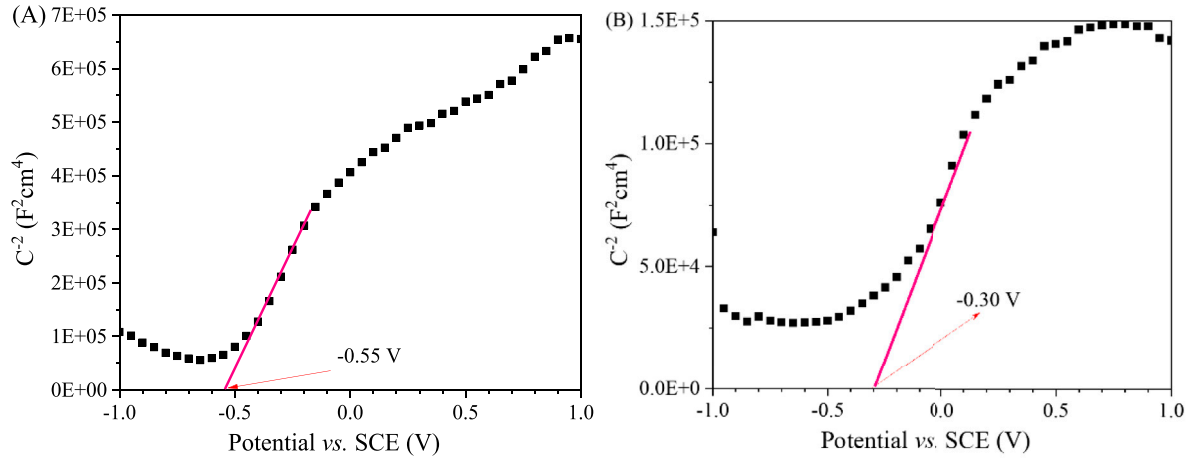

FIGURE 13
Mott-Schottky plots of $La_2(WO_4)_3$ **(A)** and $CuWO_4$ **(B)**.

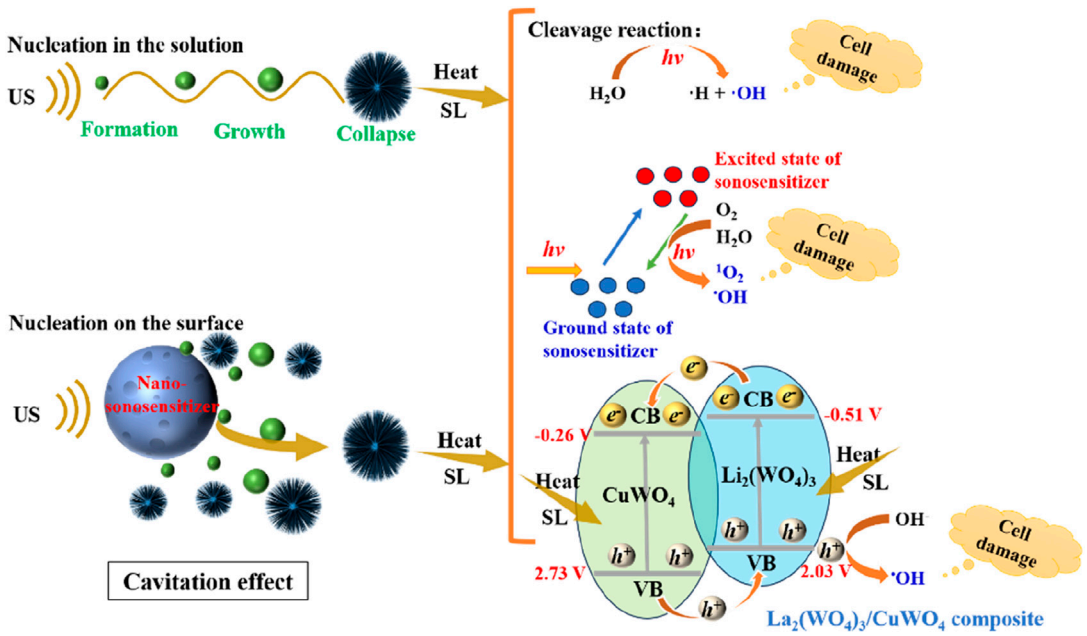

FIGURE 14
$La_2(WO_4)_3/CuWO_4$ composite mediated SDT antitumor mechanism diagram.

provide more active sites for the nucleation process and the formation of cavitation microbubbles (Qiu et al., 2018), which could generate more active free radicals, and then caused more serious damage to tumor cells. Thirdly, in the process of US irradiation, the cavitation effect of US would lead to sonoluminescence (Xu et al., 2025). The light energy generated by sonoluminescence and the heat energy from local hot spots could activate the sonosensitizer molecule to transition from the ground state to the excited state (Qian et al., 2024). In the process of the sonosensitizer molecule returning from the excited state to the ground state, the released energy was transferred to the water and oxygen molecules in the medium. ROS with strong oxidizing properties such as $^1O_2$ and ·OH were produced (Qian et al., 2024), thus causing damage to tumor cells. Finally, the $La_2(WO_4)_3/CuWO_4$ composite formed by $La_2(WO_4)_3$ and $CuWO_4$ was stimulated by the light generated by sonoluminescence and heat from local hot spots. When the light energy and the heat energy were equal to or exceeded the E_g of $La_2(WO_4)_3$ and $CuWO_4$ semiconductor, the photothermal generated e^- would produce on the VB of $La_2(WO_4)_3$ and $CuWO_4$, and then transferred to the CB, forming h^+ on the VB of $La_2(WO_4)_3$ and $CuWO_4$, respectively (Xu et al., 2025). Due to

obvious differences in the band and energy level structure between $La_2(WO_4)_3$ and $CuWO_4$ in $La_2(WO_4)_3/CuWO_4$ composite, the photothermal generated e^- on the CB of $La_2(WO_4)_3$ would transfer to the CB of $CuWO_4$, and photothermal generated h^+ on the VB of $CuWO_4$ would transfer to the VB of $La_2(WO_4)_3$. This could effectively inhibit the photothermal-generated e^-–h^+ pairs recombination in $La_2(WO_4)_3/CuWO_4$ composite. Because the E_{VB} oxidation potential (2.03 V) of $La_2(WO_4)_3$ was higher than that of ·OH/OH^- (1.99 V) (He et al., 2025; Sun et al., 2025), h^+ on VB could oxidize OH^- to ·OH, leading to oxidative damage of tumor cells. In addition, the CB reduction potential (−0.26 V) of $CuWO_4$ was not negative than that of $O_2/{\cdot}O_2^-$ (−0.33 V) (Wang et al., 2024; Sun et al., 2024), which suggested that the e^- on the CB of $CuWO_4$ could not reduce O_2 to superoxide anion radical (${\cdot}O_2^-$). In summary, the production of ROS such as $^1O_2$ and ·OH, especially the production of ·OH, played an important role in the $La_2(WO_4)_3/CuWO_4$ composite mediated SDT antitumor process, which was consistent with the results of previous ROS probe experiments.

4 Conclusion

In summary, $La_2(WO_4)_3/CuWO_4$ composites were prepared by two-step hydrothermal method and characterized by XRD, SEM, XPS, EDX and DRS. On this basis, using u251 glioma cells as model, the sonodynamic antitumor activity of $La_2(WO_4)_3/CuWO_4$ composite LC-10 was investigated by MTT method and AO/EB staining. The results showed that compared with $La_2(WO_4)_3$ and $CuWO_4$, $La_2(WO_4)_3/CuWO_4$ composite had better sonodynamic antitumor activity, and LC-10 had good biosafety at concentrations below 50 $\mu g{\cdot}mL^{-1}$. After $La_2(WO_4)_3$ and $CuWO_4$ formed $La_2(WO_4)_3/CuWO_4$ composite, the photo-thermal generated e^- on the CB of $La_2(WO_4)_3$ would be transferred to the CB of $CuWO_4$, and the generated h^+ on the VB of $CuWO_4$ would be transferred to the VB of $La_2(WO_4)_3$ during SDT. The recombination of e^-–h^+ pairs was effectively inhibited, and more strongly oxidizing ROS was produced, inducing apoptosis of u251 glioma cells. In which, $^1O_2$ and ·OH, especially the production of ·OH, played an important role in the $La_2(WO_4)_3/CuWO_4$ composite mediated SDT antitumor process. In general, the results of this study would lay a foundation for the design of $CuWO_4$ base nano-sonosensitizer and its further clinical application in the study of sonodynamic antitumor. At the same time, it also provided a new strategy for the design and development of novel nano-sonosensitizers with excellent sonodynamic activity.

Data availability statement

The original contributions presented in the study are included in the article/Supplementary Material, further inquiries can be directed to the corresponding author.

Ethics statement

Ethical approval was not required for the studies on humans in accordance with the local legislation and institutional requirements because only commercially available established cell lines were used.

Author contributions

F-YL: Data curation, Investigation, Writing–original draft. XW: Conceptualization, Methodology, Project administration, Writing–review and editing. Y-FL: Funding acquisition, Project administration, Writing–review and editing.

Funding

The author(s) declare that financial support was received for the research, authorship, and/or publication of this article. This work was financially supported by the Medical and Industrial Cross Joint Fund of Liaoning Cancer Hospital and Institute and Dalian University of Technology (LD202212).

Conflict of interest

The authors declare that the research was conducted in the absence of any commercial or financial relationships that could be construed as a potential conflict of interest.

Generative AI statement

The author(s) declare that no Generative AI was used in the creation of this manuscript.

Publisher's note

Supplementary material

The Supplementary Material for this article can be found online at: https://www.frontiersin.org/articles/10.3389/fbioe.2025.1566946/full#supplementary-material

References

Baby, B., Thomas, S., Jose, J., Thomas, K., Punathil, P., Unnikrishnan, N. V., et al. (2024). Luminescence studies and Judd Ofelt parameterization of Dy^{3+} activated $La_2(WO_4)_3$ yellow phosphor. *Inorg. Chem. Commun.* 165, 112550. doi:10.1016/j.inoche.2024.112550

Canavese, G., Ancona, A., Racca, L., Canta, M., Dumontel, B., Barbaresco, F., et al. (2018). Nanoparticle-assisted ultrasound: a special focus on sonodynamic therapy against cancer. *Chem. Eng. J.* 340, 155–172. doi:10.1016/j.cej.2018.01.060

Chang, F., Bao, W., Li, K., Bai, W., Shi, Z., Liu, D.-g., et al. (2024). Augmented photocatalytic NO removal by the S-scheme $Bi_7O_9I_3/Bi_2S_3$ heterojunctions with surface oxygen vacancies: experimental analyses and theoretical calculations. *J. Environ. Manag.* 370, 122390. doi:10.1016/j.jenvman.2024.122390

Chang, F., Lei, Y., Li, J., Li, S., Liu, D.-g., and Kong, Y. (2023). Externally modified $Bi_{12}SiO_{20}$ with BiOI: n-p heterojunctions for effectually photocatalytic degradation of bisphenol A. *Sep. Purif. Technol.* 323, 124516. doi:10.1016/j.seppur.2023.124516

Chang, F., Li, J., Kou, Y., Bao, W., Shi, Z., Zhu, G., et al. (2025). The intense charge migration and efficient photocatalytic NO removal of the S-scheme heterojunction composites $Bi_7O_9I_3$-BiOBr. *Sep. Purif. Technol.* 353, 128402. doi:10.1016/j.seppur.2024.128402

Chen, H., Sun, M., Zhao, J., Huang, X., Teng, H., Gao, Y., et al. (2024). *In-situ* assembling novel N-Ti_3C_2/$BiOCl_xBr_{1-x}$ composites with enhanced photocatalytic degradation and nitrogen reduction activity. *Spectrochimica Acta Part A Mol. Biomol. Spectrosc.* 316, 124331. doi:10.1016/j.saa.2024.124331

Chen, L., Mao, Z., Wang, Y., Kang, Y., Wang, Y., Mei, L., et al. (2022). Edge modification facilitated heterogenization and exfoliation of two-dimensional nanomaterials for cancer catalytic therapy. *Sci. Adv.* 8, eabo7372. doi:10.1126/sciadv.abo7372

Cheng, M., Liu, Y., You, Q., Lei, Z., Ji, J., Zhang, F., et al. (2024). Metal-doping strategy for carbon-based sonosensitizer in sonodynamic therapy of glioblastoma. *Adv. Sci.* 11, 2404230. doi:10.1002/advs.202404230

Cui, Y., Chen, X., Cheng, Y., Lu, X., Meng, J., Chen, Z., et al. (2021). $CuWO_4$ Nanodots for NIR-induced photodynamic and chemodynamic synergistic therapy. *ACS Appl. Mater. and Interfaces* 13, 22150–22158. doi:10.1021/acsami.1c00970

Dong, Y., Dong, S., Liu, B., Yu, C., Liu, J., Yang, D., et al. (2021). 2D piezoelectric Bi_2MoO_6 nanoribbons for GSH-enhanced sonodynamic therapy. *Adv. Mater.* 33, 2106838. doi:10.1002/adma.202106838

Duan, Y., Yu, Y., Liu, P., Gao, Y., Dai, X., Zhang, L., et al. (2023). Reticular chemistry-enabled sonodynamic activity of covalent organic frameworks for nanodynamic cancer therapy. *Angew. Chem. Int. Ed.* 62, e202302146. doi:10.1002/anie.202302146

Gong, F., Cheng, L., Yang, N., Gong, Y., Ni, Y., Bai, S., et al. (2020). Preparation of $TiH_{1.924}$ nanodots by liquid-phase exfoliation for enhanced sonodynamic cancer therapy. *Nat. Commun.* 11, 3712. doi:10.1038/s41467-020-17485-x

Hachimine, K., Shibaguchi, H., Kuroki, M., Yamada, H., Kinugasa, T., Nakae, Y., et al. (2007a). Sonodynamic therapy of cancer using a novel porphyrin derivative, DCPH-P-Na(I), which is devoid of photosensitivity. *Cancer Sci.* 98, 916–920. doi:10.1111/j.1349-7006.2007.00468.x

Hachimine, K., Shibaguchi, H., Kuroki, M., Yamada, H., Kinugasa, T., Nakae, Y., et al. (2007b). Sonodynamic therapy of cancer using a novel porphyrin derivative, DCPH-P-Na(I), which is devoid of photosensitivity. *Cancer Sci.* 98, 916–920. doi:10.1111/j.1349-7006.2007.00468.x

Han, X., Huang, J., Jing, X., Yang, D., Lin, H., Wang, Z., et al. (2018). Oxygen-deficient black titania for synergistic/enhanced sonodynamic and photoinduced cancer therapy at near infrared-II biowindow. *ACS Nano* 12, 4545–4555. doi:10.1021/acsnano.8b00899

Han, Y., Qi, X.-X., Liu, Y.-C., Wang, Y., Xiang, Z., and Wang, X. (2025). Preparation of $CuWO_4/Bi_2WO_6$ composite and its sonocatalytic removal of tetracycline by combined persulfate. *J. Alloys Compd.* 1010, 177505. doi:10.1016/j.jallcom.2024.177505

He, L.-L., Li, S., Qi, S., Wang, N., Sun, M.-T., Su, C., et al. (2024). Synthesis of three-dimensional flower-like $BiFeO_3$ with enhanced sonocatalytic performance for the removal of methylene blue. *Inorg. Chem. Commun.* 166, 112649. doi:10.1016/j.inoche.2024.112649

He, L.-L., Wang, N., Qi, S., Sun, M.-T., Kou, X.-W., Su, C., et al. (2025). Preparation of $CuWO_4/CaWO_4$ n–n heterojunction with enhanced sonocatalytic performance: characterization, sonocatalytic mechanism and degradation pathways of organic pollutant. *Inorg. Chem. Commun.* 171, 113564. doi:10.1016/j.inoche.2024.113564

He, L.-L., Wang, X., Liu, B., Wang, J., Sun, Y.-G., and Xu, S.-K. (2011a). Study on the sonodynamic activity and mechanism of promethazine hydrochloride by multi-spectroscopic techniques. *Spectrochimica Acta Part A Mol. Biomol. Spectrosc.* 81, 698–705. doi:10.1016/j.saa.2011.07.006

He, L.-L., Wang, X., Liu, B., Wang, J., Sun, Y.-G., and Xu, S.-K. (2011b). Spectroscopic investigation on the synergistic effects of ultrasound and dioxopromethazine hydrochloride on protein. *J. Fluoresc.* 21, 1847–1856. doi:10.1007/s10895-011-0879-2

He, L.-L., Wang, X., Wu, X.-X., Wang, Y.-X., Kong, Y.-M., Wang, X., et al. (2015a). Protein damage and reactive oxygen species generation induced by the synergistic effects of ultrasound and methylene blue. *Spectrochimica Acta Part A Mol. Biomol. Spectrosc.* 134, 361–366. doi:10.1016/j.saa.2014.06.121

He, L.-L., Wu, X.-X., Wang, Y.-X., Liu, X.-P., Song, Y.-L., Yang, Y.-J., et al. (2015b). Spectroscopic investigation on the sonodynamic damage to protein in the presence of eosine B. *Ultrason. Sonochemistry* 26, 93–98. doi:10.1016/j.ultsonch.2015.02.002

Huang, X., Chen, H., Sun, M., Zhao, J., Teng, H., Gao, Y., et al. (2024c). N-graphyne surrounded Bi_2S_3/BiOBr composites: in-situ ultrasound-assisted synthesis and superior photocatalytic activity. *Fuel* 375, 132613. doi:10.1016/j.fuel.2024.132613

Huang, X., Sun, M., Humayun, M., Li, S., Zhao, J., Chen, H., et al. (2024b). *In-situ* synthesis of efficient N-graphyne/Bi/BiOBr photocatalysts for contaminants removal and nitrogen fixation. *J. Alloys Compd.* 976, 173025. doi:10.1016/j.jallcom.2023.173025

Huang, X., Sun, M., Sun, W., Li, Z., Chen, H., and Zhao, J. (2024a). One-step hydrothermal formation of porous N-graphyne decorated TiO_2/Ti_3C_2 composites with enhanced photocatalytic activity. *Int. J. Hydrogen Energy* 55, 581–591. doi:10.1016/j.ijhydene.2023.11.203

Jiang, L., Wang, J., Jiang, J., Zhang, C., Zhao, M., Chen, Z., et al. (2020). Sonodynamic therapy in atherosclerosis by curcumin nanosuspensions: preparation design, efficacy evaluation, and mechanisms analysis. *Eur. J. Pharm. Biopharm.* 146, 101–110. doi:10.1016/j.ejpb.2019.12.005

Kang, Y., Mao, Z., Wang, Y., Pan, C., Ou, M., Zhang, H., et al. (2022). Design of a two-dimensional interplanar heterojunction for catalytic cancer therapy. *Nat. Commun.* 13, 2425. doi:10.1038/s41467-022-30166-1

Kumar, G., Kumar, J., Bag, M., and Kumar Dutta, R. (2022). Solar light induced photocatalytic process for reduction of hexavalent chromium and degradation of tetracycline and methylene blue by heterostructures made of SnS_2 nanoplates surface modified by $ZnWO_4$ nanorods. *Sep. Purif. Technol.* 292, 121040. doi:10.1016/j.seppur.2022.121040

Li, J.-H., Song, D.-Y., Xu, Y.-G., Huang, Z., and Yue, W. (2008). *In vitro* study of haematoporphyrin monomethyl ether-mediated sonodynamic effects on C6 glioma cells. *Neurol. Sci.* 29, 229–235. doi:10.1007/s10072-008-0972-8

Li, R., Wang, X., Shi, J., Kang, Y., and Ji, X. (2023). Sonocatalytic cancer therapy: theories, advanced catalysts and system design. *Nanoscale* 15, 19407–19422. doi:10.1039/d3nr04505f

Liu, Q., Wang, X., Wang, P., Qi, H., Zhang, K., and Xiao, L. (2006). Sonodynamic effects of protoporphyrin IX disodium salt on isolated sarcoma 180 cells. *Ultrasonics* 45, 56–60. doi:10.1016/j.ultras.2006.06.063

Liu, Y.-C., Ge, Y.-D., An, H.-L., Ju, W.-T., Zhou, X.-Y., Xing, M.-Y., et al. (2024). Synthesis of a novel double Z-scheme $BiVO_4/Cu_2O$/g-C_3N_4 sonocatalyst and research on sonocatalytic degradation of tetracycline. *J. Environ. Chem. Eng.* 12, 113668. doi:10.1016/j.jece.2024.113668

Liu, Y.-C., Liu, X., Wang, X., Li, Z.-H., Chen, C.-L., and Xiang, Z. (2023). Hybrid persulfate/sonocatalysis for degradation of acid orange 7 in the presence of Ag_2O/$CuWO_4$ composite: operating parameters and sonocatalytic mechanism. *J. Clean. Prod.* 394, 136287. doi:10.1016/j.jclepro.2023.136287

Lu, X., Li, J., and Chang, F. (2025). Sonocatalytic evaluation of binary composites $Bi_{12}GeO_{20}$/GO in degradation of tetracycline hydrochloride. *Mater. Sci. Semicond. Process.* 185, 108964. doi:10.1016/j.mssp.2024.108964

Pan, X., Bai, L., Wang, H., Wu, Q., Wang, H., Liu, S., et al. (2018). Metal–organic-framework-derived carbon nanostructure augmented sonodynamic cancer therapy. *Adv. Mater.* 30, 1800180. doi:10.1002/adma.201800180

Ping, J., Du, J., Ouyang, R., Miao, Y., and Li, Y. (2023). Recent advances in stimuli-responsive nano-heterojunctions for tumor therapy. *Colloids Surfaces B Biointerfaces* 226, 113303. doi:10.1016/j.colsurfb.2023.113303

Qian, M.-Q., Xiang, Z., and Wang, X. (2024). Sonodynamic inactivation of gram-negative and gram-positive bacteria in the presence of phenothiazine compounds toluidine blue and azurin A. *Biochimica Biophysica Acta (BBA) - General Subj.* 1868, 130711. doi:10.1016/j.bbagen.2024.130711

Qiu, P., Park, B., Choi, J., Thokchom, B., Pandit, A. B., and Khim, J. (2018). A review on heterogeneous sonocatalyst for treatment of organic pollutants in aqueous phase based on catalytic mechanism. *Ultrason. Sonochemistry* 45, 29–49. doi:10.1016/j.ultsonch.2018.03.003

Rosenthal, I., Sostaric, J. Z., and Riesz, P. (2004). Sonodynamic therapy––a review of the synergistic effects of drugs and ultrasound. *Ultrason. Sonochemistry* 11, 349–363. doi:10.1016/j.ultsonch.2004.03.004

Sasaki, K., Yumita, N., Nishigaki, R., and Umemura, S. (1998). Antitumor effect sonodynamically induced by focused ultrasound in combination with Ga-porphyrin complex. *Jpn. J. Cancer Res.* 89, 452–456. doi:10.1111/j.1349-7006.1998.tb00584.x

Song, K., Du, J., Wang, X., Zheng, L., Ouyang, R., Li, Y., et al. (2022). Biodegradable bismuth-based nano-heterojunction for enhanced sonodynamic oncotherapy through charge separation engineering. *Adv. Healthc. Mater.* 11, 2102503. doi:10.1002/adhm.202102503

Sun, L., He, X., Liu, B., Zhang, S., Xiang, Z., Wang, X., et al. (2025). Synergistic adsorption-photocatalytic degradation of tetracycline by S-scheme $InVO_4/ZnIn_2S_4$ heterojunction: mechanism, toxicity assessment, and potential applications. *Sep. Purif. Technol.* 353, 128515. doi:10.1016/j.seppur.2024.128515

Sun, M.-T., Qi, Q., Wang, X., and He, L.-L. (2024). Synthesis of $Ag_2O/CaMoO_4$ S-type heterojunction with enhanced sonocatalytic performance to remove crystal violet in dye wastewater. *Inorg. Chem. Commun.* 167, 112778. doi:10.1016/j.inoche.2024.112778

Teng, J., Xiong, S., Li, F., Wang, S., and Li, T. (2024). Sonocatalytic performance of Bi_2WO_6 nanoparticles for degradation of tetracycline antibiotics. *Appl. Catal. O Open* 191, 206957. doi:10.1016/j.apcato.2024.206957

Umemura, S., Yumita, N., Nishigaki, R., and Umemura, K. (1989). "Sonochemical activation of hematoporphyrin: a potential modality for cancer treatment," in *Ultrasonics symposium, proceedings* (IEEE), 955–960.

Umemura, S.-i., Yumita, N., and Nishigaki, R. (1993). Enhancement of ultrasonically induced cell damage by a gallium-porphyrin complex, ATX-70. *Jpn. J. Cancer Res.* 84, 582–588. doi:10.1111/j.1349-7006.1993.tb00179.x

Wan, L., Sheng, J., Chen, H., and Xu, Y. (2013). Different recycle behavior of Cu^{2+} and Fe^{3+} ions for phenol photodegradation over TiO_2 and WO_3. *J. Hazard. Mater.* 262, 114–120. doi:10.1016/j.jhazmat.2013.08.002

Wang, X., He, L.-L., Liu, B., Wang, X.-F., Xu, L., and Sun, T. (2018). Reactive oxygen species generation and human serum albumin damage induced by the combined effects of ultrasonic irradiation and brilliant cresyl blue. *Int. J. Biol. Macromol.* 120, 1865–1871. doi:10.1016/j.ijbiomac.2018.10.002

Wang, X., He, X.-S., Li, C.-Y., Liu, S.-L., Lu, W., Xiang, Z., et al. (2023b). Sonocatalytic removal of tetracycline in the presence of S-scheme $Cu_2O/BiFeO_3$ heterojunction: operating parameters, mechanisms, degradation pathways and toxicological evaluation. *J. Water Process Eng.* 51, 103345. doi:10.1016/j.jwpe.2022.103345

Wang, X., Yu, S., Li, Z.-H., He, L.-L., Liu, Q.-L., Hu, M.-Y., et al. (2021). Fabrication Z-scheme heterojunction of $Ag_2O/ZnWO_4$ with enhanced sonocatalytic performances for meloxicam decomposition: increasing adsorption and generation of reactive species. *Chem. Eng. J.* 405, 126922. doi:10.1016/j.cej.2020.126922

Wang, Y., Gong, F., Han, Z., Lei, H., Zhou, Y., Cheng, S., et al. (2023a). Oxygen-deficient molybdenum oxide nanosensitizers for ultrasound-enhanced cancer metalloimmunotherapy. *Angew. Chem. Int. Ed.* 62, e202215467. doi:10.1002/anie.202215467

Wang, Y., Li, F., and Li, T. (2024). Facile synthesis of $BiOI/BaNbO_3$ composite for rapid sonocatalytic degradation of tetracycline hydrochloride. *J. Solid State Chem.* 333, 124644. doi:10.1016/j.jssc.2024.124644

Wei, J., Li, T., and Li, F. (2023). Synthesis and sonocatalytic performance of $Dy_2Sn_2O_7$/Sepiolite nanocomposite. *J. Solid State Chem.* 328, 124368. doi:10.1016/j.jssc.2023.124368

Wu, N., Fan, C.-H., and Yeh, C.-K. (2022). Ultrasound-activated nanomaterials for sonodynamic cancer theranostics. *Drug Discov. Today* 27, 1590–1603. doi:10.1016/j.drudis.2022.02.025

Xiao, Z., Peng, C., Jiang, X., Peng, Y., Huang, X., Guan, G., et al. (2016). Polypyrrole-encapsulated iron tungstate nanocomposites: a versatile platform for multimodal tumor imaging and photothermal therapy. *Nanoscale* 8, 12917–12928. doi:10.1039/c6nr03336a

Xing, X., Zhao, S., Xu, T., Huang, L., Zhang, Y., Lan, M., et al. (2021). Advances and perspectives in organic sonosensitizers for sonodynamic therapy. *Coord. Chem. Rev.* 445, 214087. doi:10.1016/j.ccr.2021.214087

Xu, L., Ge, Y.-D., Zhou, X.-Y., Xing, M.-Y., Wu, X.-Q., Wang, Y., et al. (2025). Study on the sonocatalytic removal of tetracycline by an type-II heterojunction $CuS/FeWO_4$. *J. Alloys Compd.* 1015, 178826. doi:10.1016/j.jallcom.2025.178826

Xu, L., Wu, X.-Q., Li, C.-Y., Liu, N.-P., An, H.-L., Ju, W.-T., et al. (2023). Sonocatalytic degradation of tetracycline by $BiOBr/FeWO_4$ nanomaterials and enhancement of sonocatalytic effect. *J. Clean. Prod.* 394, 136275. doi:10.1016/j.jclepro.2023.136275

Yang, Y., Wang, X., Qian, H., and Cheng, L. (2021). Titanium-based sonosensitizers for sonodynamic cancer therapy. *Appl. Mater. Today* 25, 101215. doi:10.1016/j.apmt.2021.101215

Zhang, M., Cui, Z., Song, R., Lv, B., Tang, Z., Meng, X., et al. (2018). $SnWO_4$-based nanohybrids with full energy transfer for largely enhanced photodynamic therapy and radiotherapy. *Biomaterials* 155, 135–144. doi:10.1016/j.biomaterials.2017.11.013

Zhang, S., Xia, S., Chen, L., Chen, Y., and Zhou, J. (2023b). Covalent organic framework nanobowls as activatable nanosensitizers for tumor-specific and ferroptosis-augmented sonodynamic therapy. *Adv. Sci.* 10, 2206009. doi:10.1002/advs.202206009

Zhang, S., Zhang, L., Hu, J., He, X., Geng, B., Pan, D., et al. (2023a). Trienzyme-like $Co_3O_4@TiO_{2-x}$ nanozymes for heterojunction-enhanced nanocatalytic-sonodynamic tumor therapy. *Chem. Eng. J.* 458, 141485. doi:10.1016/j.cej.2023.141485

Zhang, T., Zheng, Q., Fu, Y., Xie, C., Fan, G., Wang, Y., et al. (2021). α-Fe_2O_3@Pt heterostructure particles to enable sonodynamic therapy with self-supplied O_2 and imaging-guidance. *J. Nanobiotechnology* 19, 358. doi:10.1186/s12951-021-01105-x

Zhou, Y., Cao, Z., Jiang, L., Chen, Y., Cui, X., Wu, J., et al. (2024). Magnetically actuated sonodynamic nanorobot collectives for potentiated ovarian cancer therapy. *Front. Bioeng. Biotechnol.* 12, 1374423. doi:10.3389/fbioe.2024.1374423

Zhou, Y., Yang, N., Gong, F., Wang, Y., Yang, X., Dai, Y., et al. (2022). Oxygen-deficient tungsten oxide (WO_x) nanobelts with pH-sensitive degradation for enhanced sonodynamic therapy of cancer. *ACS Nano* 16, 17242–17256. doi:10.1021/acsnano.2c07903

Zhu, P., Chen, Y., and Shi, J. (2020). Piezocatalytic tumor therapy by ultrasound-triggered and $BaTiO_3$-mediated piezoelectricity. *Adv. Mater.* 32, 2001976. doi:10.1002/adma.202001976